# Chapter 4
Multi-dimensional CESE Schemes

The previous chapter has shown that the necessary numerical dissipation can be introduced in 1D CESE schemes through either a central or upwind approach. In this chapter, we present the extensions of 2D CESE schemes based on cartesian meshes, followed by a detailed description of implementation on unstructured meshes. Both the central schemes and upwind schemes will be presented. Then, numerical examples will be provided to demonstrate the capabilities of the present schemes.

4.1 CESE Schemes on Cartesian Meshes

4.1.1 The Improved a-α CESE Scheme

The marching scheme requires physical variables and their spatial derivatives at each mesh point. In the pioneer development of the 2D CESE solver [1], the domain is discretized by congruent triangles. Based on a similar technique, Zhang, Yu, and Chang [2] reported a further extension of the 2D CESE scheme on quadrilateral meshes. In the above versions of CESE schemes, the solution points are solely updated at the cell centers with a staggered stencil. As a result, a generalized flux technique was also proposed as a post-marching procedure to handle the "flux decoupling" problem when two mesh points cohost one sub-CE. Alternatively, an improved 2D CESE scheme [3, 4] was proposed with a new definition of SE and CE. In this updated scheme, the entire space–time region is divided into non-overlapping CEs, making it convenient and simpler for calculation and straightforward for extension to 3D scheme. Figure 4.1 shows the space–time geometrical configuration of the improved 2D CESE scheme with a uniform rectangular mesh. The spatial projections of the solution points at $(n-1/2)$th and nth time levels are denoted as ■ and

●, respectively. The solution is updated alternatively between the cell centers ● and cell vertices ■. Here $\Delta t/2 = t_n - t_{n-1/2}$ and P, P', and P'' subsequently represent the points at three successive timesteps. The conservation element of point P', denoted by CE(P'), is defined by the space–time hexahedron $ABCDA'B'C'D'$, i.e., the union of four sub-CEs: $CE^{LD}(P')$, $CE^{LU}(P')$, $CE^{RD}(P')$, and $CE^{RU}(P')$. In particular, $CE^{LD}(P')$ is defined as $AFPEA'F'P'E'$. Other sub-CEs are defined similarly. Next, consider the solution element of P', SE(P'), which consists of three orthogonal planes, $A'B'C'D'$, $EGG''E''$, and $FHH''F''$. The physical flux vector is assumed to be smooth within each SE and can be approximated by Taylor expansions about the mesh point associated with the SE. In the following, we present the construction of the 2D CESE solver using similar techniques as described in the 1D scheme.

(a) Mesh points on the *x-y* plane

(b) CE(P')

(c) SE(P')

(d) Fluxes in the sub-CEs
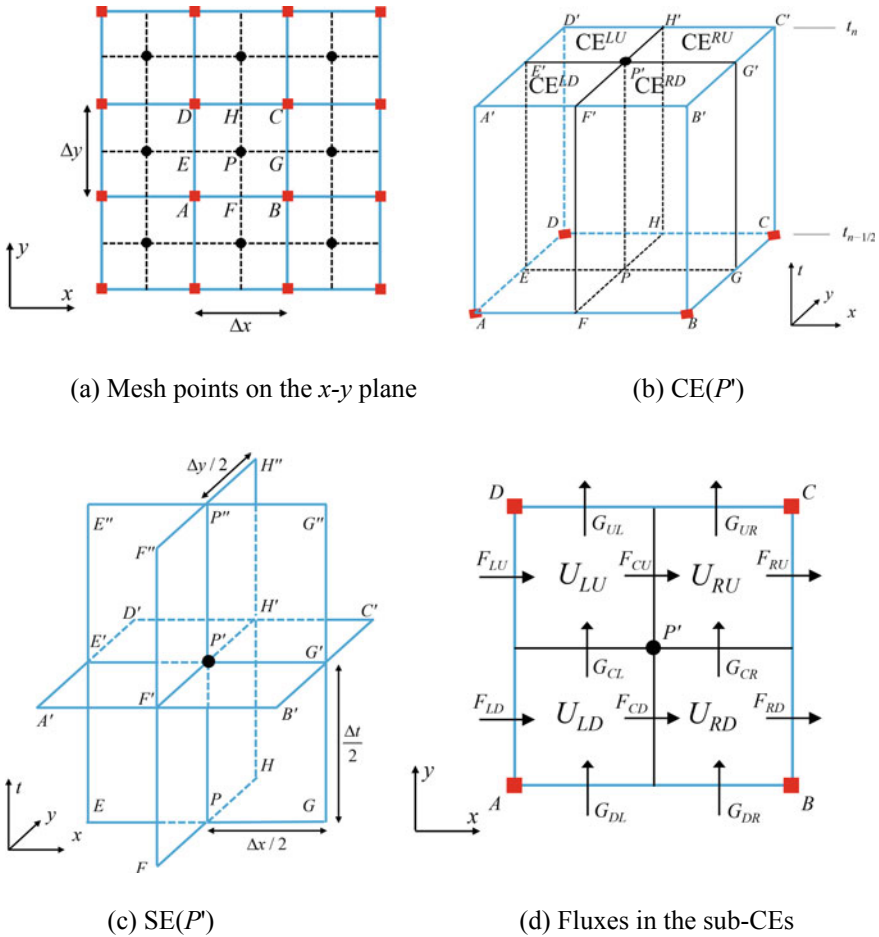
Fig. 4.1 Grid points in the spatial domain, definitions of CE and SE, and corresponding fluxes in a CE for the 2D CESE scheme on rectangular meshes

In this section, we consider the 2D scalar hyperbolic conservation law

$$\frac{\partial u}{\partial t} + \frac{\partial f}{\partial x} + \frac{\partial g}{\partial y} = 0. \tag{4.1}$$

By using the Gauss' divergence theorem, it is shown that Eq. (4.1) can be written in the form of

$$\oint_{S(CE(P'))} \boldsymbol{h} \cdot \boldsymbol{n} \, \mathrm{d}S = 0, \tag{4.2}$$

where $\boldsymbol{h} = (f, g, u)$ is the space–time flux vector, $S\big(CE(P')\big)$ is the boundary of $CE(P')$, $\boldsymbol{n}$ is the unit outward normal vector on the surface of the control volume. Note that the u, f, and g are approximated by first-order Taylor expansion about point P'. For any $(x, y, t) \in SE(P')$, let

$$u(x, y, t) = u(\delta x, \delta y, \delta t)_{P'}, \tag{4.3}$$

$$f(x, y, t) = f(\delta x, \delta y, \delta t)_{P'}, \tag{4.4}$$

$$g(x, y, t) = g(\delta x, \delta y, \delta t)_{P'}, \tag{4.5}$$

where $X(\delta x, \delta y, \delta t)_N$ denotes the first-order Taylor expansion about point N as

$$X(\delta x, \delta y, \delta t)_N = X_N + (X_x)_N \delta x + \big(X_y\big)_N \delta y + (X_t)_N \delta t, \tag{4.6}$$

and

$$\delta x = x - x_N, \quad \delta y = y - y_N, \quad \delta t = t - t_N. \tag{4.7}$$

In addition, the spatial and temporal derivatives of $f(u)$ and $g(u)$ can be derived by the chain rule (Eqs. (2.26) and (2.28)) and $u_t = -f_x - g_y$.

Meanwhile, one obtains local flux conservation of the four sub-CEs by integrating Eq. (4.2) over their surfaces, given by

$$U'_{LD} \frac{\Delta x \Delta y}{4} = U_{LD} \frac{\Delta x \Delta y}{4} + (F_{LD} - F_{CD}) \frac{\Delta y \Delta t}{4} + (G_{DL} - G_{CL}) \frac{\Delta x \Delta t}{4}, \tag{4.8}$$

$$U'_{RD} \frac{\Delta x \Delta y}{4} = U_{RD} \frac{\Delta x \Delta y}{4} + (F_{CD} - F_{RD}) \frac{\Delta y \Delta t}{4} + (G_{DR} - G_{CR}) \frac{\Delta x \Delta t}{4}, \tag{4.9}$$

$$U'_{RU} \frac{\Delta x \Delta y}{4} = U_{RU} \frac{\Delta x \Delta y}{4} + (F_{CU} - F_{RU}) \frac{\Delta y \Delta t}{4} + (G_{CR} - G_{UR}) \frac{\Delta x \Delta t}{4},$$

(4.10)

$$U'_{LU} \frac{\Delta x \Delta y}{4} = U_{LU} \frac{\Delta x \Delta y}{4} + (F_{LU} - F_{CU}) \frac{\Delta y \Delta t}{4} + (G_{CL} - G_{UL}) \frac{\Delta x \Delta t}{4},$$

(4.11)

where U_{LD}, U'_{LD}, F_{LD}, F_{CD}, G_{DL}, and G_{CL} are the average fluxes on the surfaces of CE$^{LD}(P')$, *AFPE*, *A'F'P'E'*, *AEE'A'*, *FPP'F'*, *AFF'A'*, and *EPP'E'*, respectively. Similar definitions are applied to the other sub-CEs. By definition, the fluxes U_{LD}, F_{LD}, and G_{DL} can be determined via the Taylor expansion in SE(A). It is also important to emphasize that the fluxes F_{CD} and G_{CL} that denote the fluxes across the "inner" surface of two neighboring sub-CEs, however, are not trivially available due to the presence of discontinuities. In fact, it will be shown later that all the fluxes across the interfaces among sub-CEs vanish in the formulation of the time marching scheme of *u*. Apart from this, based on the assumption that the distribution within each SE is linear, the average fluxes on the exterior surfaces of CE$^{LD}(P')$ read

$$U_{LD} = u\left(\frac{\Delta x}{4}, \frac{\Delta y}{4}, 0\right)_A$$

(4.12)

$$U'_{LD} = u\left(-\frac{\Delta x}{4}, -\frac{\Delta y}{4}, 0\right)_{P'}$$

(4.13)

$$G_{DL} = g\left(\frac{\Delta x}{4}, 0, \frac{\Delta t}{4}\right)_A$$

(4.14)

$$F_{LD} = g\left(0, \frac{\Delta y}{4}, \frac{\Delta t}{4}\right)_A$$

(4.15)

Fluxes are expressed similarly for the other three sub-CEs.

To proceed, by adding Eqs. (4.8)–(4.11), the fluxes through the interfaces between sub-CEs are well balanced. Consequently, the value of the solution point *P'* can be derived as

$$u(P') = \frac{1}{4}(U_{LD} + U_{RD} + U_{RU} + U_{LU}) + \frac{\Delta t}{4\Delta x}(F_{LD} - F_{RD} - F_{RU} + F_{LU})$$
$$+ \frac{\Delta t}{4\Delta y}(G_{LD} + G_{RD} - G_{RU} - G_{LU})$$

(4.16)

Moreover, by replacing the average fluxes in Eq. (4.16) with the Taylor expansions about their corresponding SEs centers, we can obtain the explicit time marching scheme for *u(P')* as

$$u(P') = \frac{1}{4}\bar{u} + \frac{\Delta t}{4\Delta x}\bar{f} + \frac{\Delta t}{4\Delta y}\bar{g}, \tag{4.17}$$

where

$$\bar{u} = u\left(\frac{\Delta x}{4}, \frac{\Delta y}{4}, 0\right)_A + u\left(-\frac{\Delta x}{4}, \frac{\Delta y}{4}, 0\right)_B + u\left(-\frac{\Delta x}{4}, -\frac{\Delta y}{4}, 0\right)_C + u\left(\frac{\Delta x}{4}, -\frac{\Delta y}{4}, 0\right)_D,$$

$$\bar{f} = f\left(0, \frac{\Delta y}{4}, \frac{\Delta t}{4}\right)_A + f\left(0, -\frac{\Delta y}{4}, \frac{\Delta t}{4}\right)_D - f\left(0, \frac{\Delta y}{4}, \frac{\Delta t}{4}\right)_B - f\left(0, -\frac{\Delta y}{4}, \frac{\Delta t}{4}\right)_C,$$

$$\bar{g} = g\left(\frac{\Delta x}{4}, 0, \frac{\Delta t}{4}\right)_A + g\left(-\frac{\Delta x}{4}, 0, \frac{\Delta t}{4}\right)_B - g\left(-\frac{\Delta x}{4}, 0, \frac{\Delta t}{4}\right)_C - g\left(\frac{\Delta x}{4}, 0, \frac{\Delta t}{4}\right)_D.$$

With respect to the spatial derivatives, by using the continuous assumptions at points A', B', C', and D', the following relations can be formulated

$$u\left(-\frac{\Delta x}{2}, -\frac{\Delta y}{2}, 0\right)_{p'} = u\left(0, 0, \frac{\Delta t}{2}\right)_A, \tag{4.18}$$

$$u\left(\frac{\Delta x}{2}, -\frac{\Delta y}{2}, 0\right)_{p'} = u\left(0, 0, \frac{\Delta t}{2}\right)_B, \tag{4.19}$$

$$u\left(\frac{\Delta x}{2}, \frac{\Delta y}{2}, 0\right)_{p'} = u\left(0, 0, \frac{\Delta t}{2}\right)_C, \tag{4.20}$$

$$u\left(-\frac{\Delta x}{2}, \frac{\Delta y}{2}, 0\right)_{p'} = u\left(0, 0, \frac{\Delta t}{2}\right)_D. \tag{4.21}$$

After mathematical manipulation of Eqs. (4.19) and (4.20), (4.18) and (4.21), (4.20) and (4.21), (4.18) and (4.19), respectively, the spatial derivatives at solution point P' can be explicitly calculated as

$$u_x^+(P') = \frac{1}{\Delta x}\left[u\left(0, 0, \frac{\Delta t}{2}\right)_B + u\left(0, 0, \frac{\Delta t}{2}\right)_C - 2u(P')\right], \tag{4.22}$$

$$u_x^-(P') = -\frac{1}{\Delta x}\left[u\left(0, 0, \frac{\Delta t}{2}\right)_A + u\left(0, 0, \frac{\Delta t}{2}\right)_D - 2u(P')\right], \tag{4.23}$$

$$u_y^+(P') = \frac{1}{\Delta y}\left[u\left(0, 0, \frac{\Delta t}{2}\right)_C + u\left(0, 0, \frac{\Delta t}{2}\right)_D - 2u(P')\right], \tag{4.24}$$

$$u_y^-(P') = -\frac{1}{\Delta y}\left[u\left(0, 0, \frac{\Delta t}{2}\right)_A + u\left(0, 0, \frac{\Delta t}{2}\right)_B - 2u(P')\right]. \tag{4.25}$$

One note that, two derivatives were estimated along both spatial directions (denoted by superscripts $+$ and $-$). Recall that to a weighted averaged function Eq. (3.6) is again adopted to suppress numerical wiggles, such that

$$u_x(P') = W\big((u_x^-)_{P'}, (u_x^+)_{P'}, \alpha\big), \tag{4.26}$$

$$u_y(P') = W\big((u_y^-)_{P'}, (u_y^+)_{P'}, \alpha\big). \tag{4.27}$$

The Eqs. (4.17) and (4.22)–(4.27) constitute the first half-step marching scheme from cell vertices to cell centers. The second half-step scheme that marches from centers to vertices follows a similar approach. As described above, constructing the improved 2D a–α CESE scheme based on rectangular grids is genuinely simple and could be straightforwardly extended to the 3D scheme.

4.1.2   CNI CESE Scheme

When applying the above 2D a–α schemes [1–4] for solving problems with highly non-uniform meshes, the local CFL number may vary significantly from its stability limit of 1 to approaching 0. Namely, the solutions tend to smear out by decreasing the CFL number. The Courant number insensitive (CNI) scheme was proposed to address this issue to alleviate the sensitivity problem by improving the strategy in updating the derivatives [5]. A new point, I_m, is designated dynamically moving along the line segment connecting the vertices and the centers M'_m of each sub-CEs (Fig. 4.2). Analogous to the 1D CNI scheme (Sect. 3.2), if we define the local and global Courant numbers as ν and ν_0, the interpolated points are designated to approach the centers when $\nu/\nu_0 \to 0$, and approach the cell vertices when $\nu/\nu_0 \to 1$.

For example, the coordinates of I'_1 are

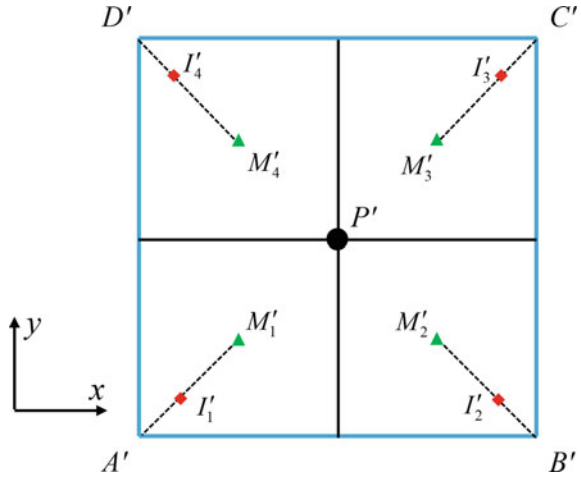$$x(I'_1) = \frac{\nu}{\nu_0}x(A') + \left(1 - \frac{\nu}{\nu_0}\right)x(M'_1), \tag{4.28}$$

$$y(I'_1) = \frac{\nu}{\nu_0}y(A') + \left(1 - \frac{\nu}{\nu_0}\right)y(M'_1). \tag{4.29}$$

If we approximate $u(I'_1)$ at $t = t_n$ from the expansions about A at $t = t_{n-1/2}$ and P' at $t = t_n$ as

$$u(\delta x_+, \delta y_+, 0)_{P'} = u(I'_1) = u\left(\delta x_-, \delta y_-, \frac{\Delta t}{2}\right)_A \tag{4.30}$$

where $\delta x_+ = x(I'_1) - x(P')$, $\delta y_+ = y(I'_1) - y(P')$, $\delta x_- = x(I'_1) - x(A)$, and $\delta y_- = y(I'_1) - y(A)$. Similar relations can be derived for each I'_m. Combining Eq. (4.30)

Fig. 4.2 Definition of points in 2D CNI CESE scheme

for $u(I_1')$ and that for $u(I_4')$, one can explicitly formulate two independent conditions for calculating the spatial derivatives of $u(P')$. Repeating the same procedure for combinations of $u(I_2')$ and $u(I_3')$, $u(I_1')$ and $u(I_2')$, $u(I_3')$ and $u(I_4')$, we arrive at four sets of spatial derivatives. The weighted average function is then used to calculate the optimal derivatives for capturing the discontinuities.
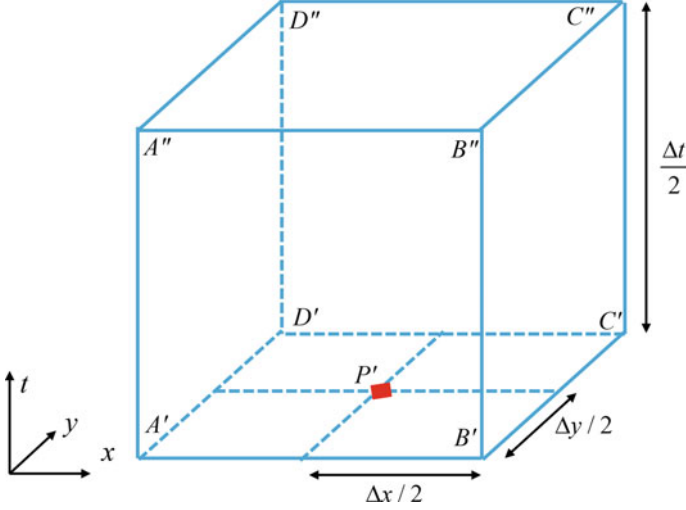
4.1.3 Upwind CESE Scheme

In the 2D upwind CESE scheme that Shen et al. [6] proposed, the CE retains the same form as the central CESE scheme. The time marching scheme of u is the same as in the a-α scheme. The upwind procedure only affects the calculation of the spatial derivatives, and global space–time conservation is ensured. In analogue to the definition in the 1D upwind scheme, for example, SE(P') is defined as cuboid $A'B'C'D'A''B''C''D''$ (Fig. 4.3), where the physical flux vector is approximated by the Taylor expansion about point P'. The average values at the top surfaces of the four sub-CEs of CE(P') read

$$U_{LD}' = u\left(-\frac{\Delta x}{4}, -\frac{\Delta y}{4}, 0\right)_{P'}, \tag{4.31}$$

$$U_{RD}' = u\left(\frac{\Delta x}{4}, -\frac{\Delta y}{4}, 0\right)_{P'}, \tag{4.32}$$

$$U_{RU}' = u\left(\frac{\Delta x}{4}, \frac{\Delta y}{4}, 0\right)_{P'}, \tag{4.33}$$

Fig. 4.3 Definition of SE of the upwind CESE scheme

$$U'_{LU} = u\left(-\frac{\Delta x}{4}, \frac{\Delta y}{4}, 0\right)_{P'}. \tag{4.34}$$

Referring to Fig. 4.1d, by substituting Eqs. (4.31) in (4.8), (4.32) in (4.9) and subtracting the two, one obtains

$$u_x^D(P') = \frac{2}{\Delta x}\left[(U_{RD} - U_{LD}) + \frac{\Delta t}{\Delta x}(2F_{CD} - F_{LD} - F_{RD}) + \frac{\Delta t}{\Delta y}(G_{DR} - G_{CR} - G_{DL} + G_{CL})\right]. \tag{4.35}$$

Equation (4.35) represents the spatial derivative in the x direction based on the information of the lower pair of CEs. Note that in contrast to central schemes, the upwind scheme requires additional estimations of inner fluxes (e.g., F_{CD}, G_{CR}, and G_{CL} in Eq. (4.35)) to compute spatial derivatives. Analogously, with the aid of Eqs. (4.31) and (4.34) and by combining with Eqs. (4.10) and (4.11), Eqs. (4.8) and (4.11), Eqs. (4.9) and (4.10), respectively. The following equations for spatial derivatives can be formulated

$$u_x^U(P') = \frac{2}{\Delta x}\left[(U_{RU} - U_{LU}) + \frac{\Delta t}{\Delta x}(2F_{CU} - F_{LU} - F_{RU}) + \frac{\Delta t}{\Delta y}(G_{CR} - G_{UR} - G_{CL} + G_{UL})\right], \tag{4.36}$$

$$u_y^L(P') = \frac{2}{\Delta y}\left[(U_{LU} - U_{LD}) + \frac{\Delta t}{\Delta x}(F_{LU} - F_{CU} - F_{LD} + F_{CD}) + \frac{\Delta t}{\Delta y}(2G_{CL} - G_{DL} - G_{UL})\right], \tag{4.37}$$

$$u_y^R(P') = \frac{2}{\Delta y}\left[(U_{RU} - U_{RD}) + \frac{\Delta t}{\Delta x}(F_{CU} - F_{RU} - F_{CD} + F_{RD}) + \frac{\Delta t}{\Delta y}(2G_{CR} - G_{DR} - G_{UR})\right]. \tag{4.38}$$

The final spatial derivatives are calculated by using WBAP limiter to remove small noises near the strong discontinuities, e.g.,

$$u_x(P') = u_x^C(P')WBAP^{L2}(1, \theta_1, \theta_2) = \frac{1}{2}\Big[u_x^D(P') + u_x^U(P')\Big]WBAP^{L2}(1, \theta_1, \theta_2), \tag{4.39}$$

where

$$\theta_1 = u_x^D(P')/u_x^C(P'),$$

$$\theta_2 = u_x^U(P')/u_x^C(P').$$

In the expressions for spatial derivatives in Eqs. (4.35)–(4.38), the fluxes on CE(P') surfaces can be easily approximated by the Taylor expansions of the values from $t = t_{n-1/2}$. To complete Eqs. (4.35)–(4.38), the fluxes through the inner boundaries of CE(P'), F_{CD}, F_{CU}, G_{CL}, and G_{CR}, need to be solved. However, the points at the two sides of the interface between two sub-CEs belong to different SEs. In that case, the fluxes across these interfaces may be discontinuous. For this reason, they can be calculated by an upwind procedure. For example,

$$F_{CD} = \widehat{F}\big(u_{CD}^-, u_{CD}^+\big), \tag{4.40}$$

where $\widehat{F}$ refers to any efficient Riemann solver, u_{CD}^- and u_{CD}^+ denote the values at the centroid of the interface $FPP'F'$, and they are respectively approximated by

$$u_{CD}^- = U_{LD} + \big(u_x^*\big)_{LD}\frac{\Delta x}{4} + \big(u_t^*\big)_{LD}\frac{\Delta t}{4} \tag{4.41}$$

$$u_{CD}^+ = U_{RD} - \big(u_x^*\big)_{RD}\frac{\Delta x}{4} + \big(u_t^*\big)_{RD}\frac{\Delta t}{4} \tag{4.42}$$

As an analogue to the 1D upwind CESE scheme, reconstructed slopes are employed in the calculation of the upwind fluxes to eliminate the spurious oscillations:

$$\big(u_x^*\big)_{LD} = u_x(A)WBAP^{L2}\big(1, \theta_{LD}^1, \theta_{LD}^2\big) \tag{4.43}$$

$$\big(u_x^*\big)_{RD} = u_x(B)WBAP^{L2}\big(1, \theta_{RD}^1, \theta_{RD}^2\big) \tag{4.44}$$

where the parameters in WBAP limiter are

$$\begin{aligned}
\theta_{LD}^1 &= \frac{(U_{RD} - U_{LD})/(\Delta x/2)}{u_x(A)}, \quad \theta_{LD}^2 = \frac{u_x(B)}{u_x(A)}, \\
\theta_{RD}^1 &= \frac{(U_{RD} - U_{LD})/(\Delta x/2)}{u_x(B)}, \quad \theta_{RD}^2 = \frac{u_x(A)}{u_x(B)}.
\end{aligned} \tag{4.45}$$

The temporal derivatives are hereafter calculated by the chain rule and Eq. (4.1),

$$\left(u_t^*\right)_{LD} = -f_x\left(U_{LD}, \left(u_x^*\right)_{LD}\right) - g_y\left(U_{LD}, u_y(A)\right) \tag{4.46}$$

$$\left(u_t^*\right)_{RD} = -f_x\left(U_{RD}, \left(u_x^*\right)_{RD}\right) - g_y\left(U_{RD}, u_y(B)\right) \tag{4.47}$$

4.2   CESE Schemes on Unstructured Meshes

In order to extend the capability of the CESE scheme to solve problems with complex spatial geometries, CESE schemes on unstructured meshes have been proposed and developed. Notably, both central and upwind versions have been developed for hybrid meshes of triangular and quadrilateral elements. Hereafter, the second order CESE scheme on hybrid meshes [7] is presented here.

4.2.1   a-α CESE Scheme

Consider a 2D mesh consisting of quadrilateral and triangular elements as sketched in Fig. 4.4. The V_i denotes the vertices of the cells. Initially, the value of u, and its spatial derivatives, u_x and u_y, are provided at these vertices. For each cell, C_m represents its centroid, and O_m is the mid-point of the cell edge. Meanwhile, V_i, $V_i^{'}$, and $V_i^{''}$ denote points at time step $t_{n-1/2}$, t_n, $t_{n+1/2}$, respectively. Other space–time points are defined similarly.

The staggered marching strategy is again adopted here. The scheme marches from vertices $V_i^{'}$ to cell centroids $C_m^{''}$ from $t = t_n$ to $t = t_{n+1/2}$. The corresponding CE for $C_m^{''}$ is either a triangular prism or a hexahedron (Fig. 4.4c and d). SE$\left(C_m^{''}\right)$) is defined as four (e.g., SE$\left(C_1^{'}\right)$) or five (e.g., SE$\left(C_2^{''}\right)$) planes intersecting at the centers. Similarly, in the other half marching step, from $t = t_{n-1/2}$ to $t = t_n$, C_m and O_m form a polygonal element of which the centroid is denoted as G_i, and the scheme marches from C_m to the G_i. Note that G_i does not necessarily coincide with V_i. Thus, interpolation is required at each marching step. SE$(V_i^{'})$ is defined as M vertical planes and one horizontal plane intersecting at $V_i^{'}$, where M denotes the number of C_m linked to CE(V_i). Each CE is composed of a group of hexahedral sub-CEs. As shown in Fig. 4.5, $O_{m-1}C_mO_mV_iO_{m-1}^{'}C_m^{'}O_m^{'}V_i^{'}$ is the mth sub-CE belonging to CE$(V_i^{'})$, $\tilde{G}_m$ and $\tilde{G}_m^{'}$ are defined as the centroids of the bottom surface $O_{m-1}C_mO_mV_i$ and top surface $O_{m-1}^{'}C_m^{'}O_m^{'}V_i^{'}$, respectively.

(a) A hybrid mesh

(b) CE(V_1) and SE(V_1)

(c) CE(C_1)

(d) CE(C_2)
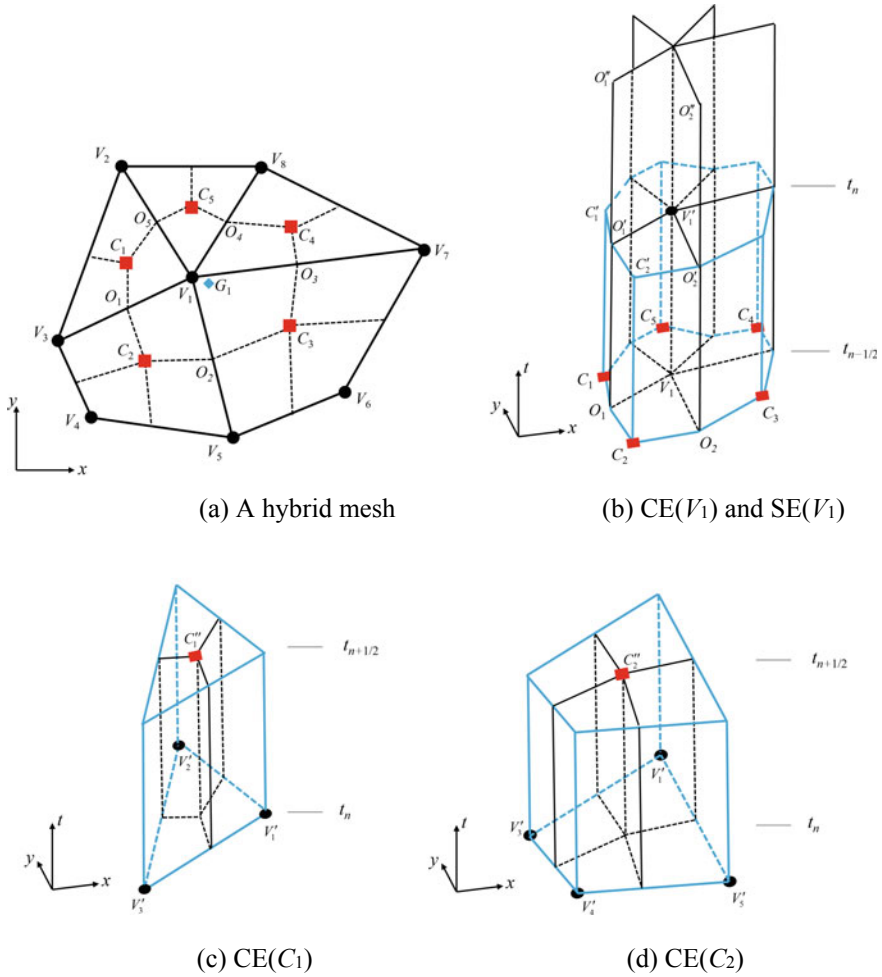
Fig. 4.4 Definition of conservation elements in CESE schemes based on a hybrid mesh

It should be noted that the marching scheme from $t = t_n$ to $t = t_{n+1/2}$ is a particular case of that from $t = t_{n-1/2}$ to $t = t_n$. From $t = t_n$ to $t = t_{n+1/2}$, the projection of a CE on the spatial domain is either a quadrilateral or a triangle, while the projection in the other step is a polygon with an arbitrary shape. Without loss of generality, we present the marching scheme from $t = t_{n-1/2}$ to $t = t_n$. By applying the integral conservation law Eq. (4.1) to the mth sub-CE, the flux-balancing relation is obtained as

$$\iint_{O'_{m-1}C'_m O'_m V'_i} u \, d\sigma = \iint_{O_{m-1}C_m O_m V_i} u \, d\sigma - \iint_{\substack{O_{m-1}C_m C'_m O'_{m-1}+C_m O_m O'_m C'_m \\ +O_{m-1}V_i V'_i O'_{m-1}+O_m V_i V'_i O'_m}} \mathbf{V} \cdot \mathbf{n} \, d\sigma, \quad (4.48)$$
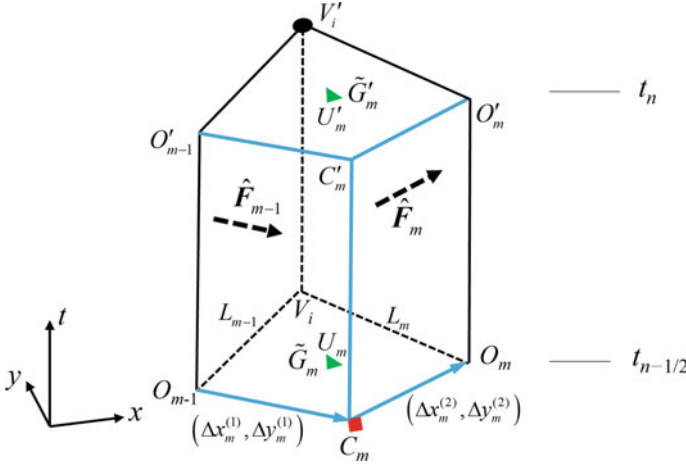
Fig. 4.5 The mth sub-CE of CE(V_i)

where $\mathbf{V} = (f, g)$ is the vector of the fluxes, and $\mathbf{n}$ is the unit outward normal vector of the surface. In second-order schemes, the integration over a surface is equivalent to the average value at the centroid multiplied by the surface area. Therefore, the above equation can be rewritten as

$$U'_m = U_m - \frac{\Delta t}{2S_m} \sum_{l=1}^{2} \left(\Delta y_m^{(l)} F_m^{(l)} - \Delta x_m^{(l)} G_m^{(l)} \right) + \frac{\Delta t}{2S_m} \left(L_{m-1} \widehat{F}_{m-1} - L_m \widehat{F}_m \right),$$

(4.49)

where S_m denotes the area of the top surface, and $\Delta t/2 = t_n - t_{n-1/2}$. U'_m, U_m, $(F_m^{(1)}, G_m^{(1)})$, and $(F_m^{(2)}, G_m^{(2)})$ represent the average values over $O'_{m-1}C'_m O'_m V'_i$, $O_{m-1}C_m O_m V_i$, $O_{m-1}C_m C'_m O'_{m-1}$, and $C_m O_m O'_m C'_m$, respectively. They can be approximated by first-order Taylor expansion in the corresponding SEs. $\widehat{F}_{m-1}$ and $\widehat{F}_m$ are the fluxes in the normal direction across the interfaces $O_{m-1} V_i V'_i O'_{m-1}$ and $O_m V_i V'_i O'_m$ with the neighbouring sub-CEs. L_{m-1} and L_m are the lengths of the line segments $O_{m-1} V_i$ and $O_m V_i$, respectively. The summation of the flux-balancing equations of every sub-CEs is expressed as

$$\iint\limits_{C'_1 O'_2 C'_2 \dots C'_M} u \, d\sigma = \sum_{m=1}^{M} \iint\limits_{O'_{m-1} C'_m O'_m V'_i} u \, d\sigma$$

(4.50)

where $O_0 \equiv O_M$. By substituting Eqs. (4.48) and (4.49) into (4.50), the interface fluxes between sub-CEs are cancelled, the conservation law on the entire CE(V'_i) yields

$$u(G_i') = \left[\sum_{m=1}^{M} U_m S_m - \frac{\Delta t}{2} \sum_{m=1}^{M} \sum_{l=1}^{2} \left(\Delta y_m^{(l)} F_m^{(l)} - \Delta x_m^{(l)} G_m^{(l)} \right) \right] \bigg/ \sum_{m=1}^{M} S_m \quad (4.51)$$

Equation (4.51) is the explicit marching scheme for $u(G_i')$. In addition, the treatment of spatial derivatives is similar to that in cartesian meshes. By using the continuous assumption at C_m', the following relation can be established

$$u(C_m) + u_t(C_m) \frac{\Delta t}{2} = u(C_m') = u(G_i') + u_x(G_i')\delta x_m + u_y(G_i')\delta y_m \quad (4.52)$$

for each m, where $\delta x_m = x(C_m) - x(G_i)$, and $\delta y_m = y(C_m) - y(G_i)$. Apply the same relation at C_{m+1}', together with Eq. (4.52), the two spatial derivatives are ready to be solved using Cramer's rule,

$$u_x(G_i') = \frac{\begin{vmatrix} \delta u_m & \delta y_m \\ \delta u_{m+1} & \delta y_{m+1} \end{vmatrix}}{\begin{vmatrix} \delta x_m & \delta y_m \\ \delta x_{m+1} & \delta y_{m+1} \end{vmatrix}}, \quad u_y(G_i') = \frac{\begin{vmatrix} \delta x_m & \delta u_m \\ \delta x_{m+1} & \delta u_{m+1} \end{vmatrix}}{\begin{vmatrix} \delta x_m & \delta y_m \\ \delta x_{m+1} & \delta y_{m+1} \end{vmatrix}}, \quad (4.53)$$

where

$$\delta u_m = u(C_m) + u_t(C_m) \frac{\Delta t}{2} - u(G_i'). \quad (4.54)$$

Totally, M pairs of derivatives can be calculated in this approach. Shen et al. [7] suggested using the weighted average function to obtain the final derivatives as

$$u_x(G_i') = \frac{\sum_{m=1}^{M} W^{(m)} u_x^{(m)}(G')}{\sum_{m=1}^{M} W^{(m)}}, \quad u_y(G_i') = \frac{\sum_{m=1}^{M} W^{(m)} u_y^{(m)}(G')}{\sum_{m=1}^{M} W^{(m)}}, \quad (4.55)$$

where

$$W^{(m)} = \left(\prod_{i=1, \, i \neq m}^{M} \sqrt{\left[u_x^{(i)}(G')_i \right]^2 + \left[u_y^{(i)}(G')_i \right]^2} \right)^{\alpha} \quad (4.56)$$

Here, the adjustable variable α ($\alpha = 0 \sim 2$) controls the dissipation near the discontinuities. Smaller α results in lower dissipation, and the function will reduce to an arithmetic average when $\alpha = 0$. Finally, the value at V_i' is interpolated from G_i' as

$$u(V_i') = u(G_i') + u_x(G_i')\left[x(V_i') - x(G_i')\right] + u_y(G_i')\left[y(V_i') - y(G_i')\right]. \quad (4.57)$$

The a–α CESE scheme on the hybrid mesh formulated by Eqs. (4.51) and (4.57), while robust, is nevertheless sensitive to the Courant number. The following section addresses the further improvements to make the scheme Courant number insensitive, including the CNI scheme and upwind scheme. These two updated schemes, being closely analogous to those presented in Sects. 4.1.2 and 4.1.3, possess the identical time-marching scheme for u as provided in the a-α CESE scheme on a hybrid mesh. Only the marching scheme for spatial derivatives is modified accordingly.

4.2.2 CNI CESE Scheme

As a straightforward extension of the 1D CNI scheme, Shen and Parsani [8] extended the CNI scheme to a hybrid mesh. Recall that the central idea of the CNI scheme is that when the local Courant number (ν) approaches the global Courant number (ν_0), the scheme becomes the a-α scheme. When ν approaches 0, the scheme reduces to the non-dissipative counterpart. As depicted in Fig. 4.6, a new point I'_m is defined such that

$$x(I'_m) = \frac{\nu}{\nu_0}x(C'_m) + \left(1 - \frac{\nu}{\nu_0}\right)x(\tilde{G}'_m), \qquad (4.58)$$

$$y(I'_m) = \frac{\nu}{\nu_0}y(C'_m) + \left(1 - \frac{\nu}{\nu_0}\right)y(\tilde{G}'_m). \qquad (4.59)$$

The value of I'_m can be obtained using the expansion from G'_i as

$$u(I'_m) = u\big(x(I'_m) - x(G'_i), y(I'_m) - y(G'_i), 0\big)_{G'_i}, \qquad (4.60)$$

Fig. 4.6 Definition of points in instructed mesh for CNI scheme
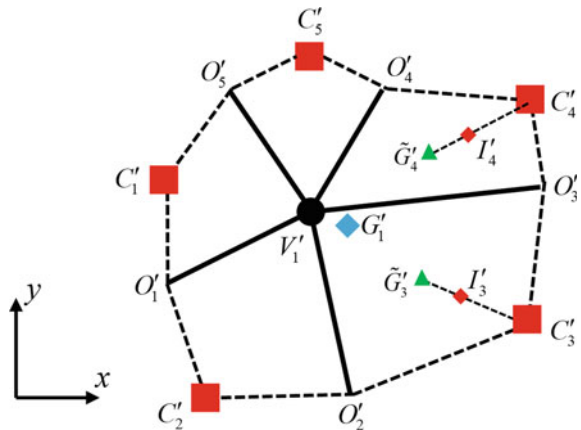
where $u(I'_m)$ can be calculated as

$$u(I'_m) = u\left(x(I'_m) - x(C_m), \, y(I'_m) - y(C_m), \, \frac{\Delta t}{2}\right)_{C_m}. \tag{4.61}$$

With the aid of Eqs. (4.60) and (4.61) to each I'_m. Every two neighboring I'_m explicitly provide one set of $u_x(G'_i)$ and $u_y(G'_i)$. Then, the optimal derivatives can be weightedly averaged from these M sets of derivatives.

4.2.3 Upwind CESE Scheme

In the upwind CESE scheme, the definition of SE is modified and $SE(V_i)$ is the polyhedron $C'_1 O'_1 C'_2...C'_M O'_M C''_1 P'' O''_1 C''_2...C''_M O''_M$ (Fig. 4.4b). The values of u, f, and g are continuous within each SE. However, the interface flux $\widehat{F}_m$ between two neighboring sub-CEs may be discontinuous. The flux $\widehat{F}_m$ can be evaluated in an upwind manner in the normal direction as

$$\hat{F}_m = \hat{F}(u_L, u_R) \tag{4.62}$$

where $\hat{F}$ denotes the Riemann solver, and the values at the center of the interface, u_L and u_R, are reconstructed from $SE(C_m)$ and $SE(C_{m+1})$ with a similar procedure as the 2D upwind CESE scheme on a uniform mesh. The WBAP limiter (Eq. (3.42)) is used to reconstruct the derivatives. Once the fluxes across inner interfaces are determined, the averaged value on the top surface of mth sub-CE U'_m in Eq. (4.49) can be explicitly computed. We can therefore relate U'_m to $u(G'_i)$ using the Taylor expansion as

$$U'_m = u(G'_i) + u_x(G'_i)\big[x(G'_m) - x(G'_i)\big] + u_y(G'_i)\big[y(G'_m) - y(G'_i)\big] \tag{4.63}$$

Two linear equations can be derived for each set of m and $m + 1$. Accordingly, a similar procedure for averaging the derivatives in the central scheme can be directly applied here.

4.3 Numerical Examples

Two canonical problems are selected to demonstrate the performance of the a–α, CNI, and upwind CESE schemes on either structured or unstructured meshes. For Euler equations, the above schemes can be directly applied to solve each component of the conserved variables. The interface fluxes in the upwind CESE scheme can be solved as a Riemann problem, where Riemann solvers including Harten, Lax and van Leer (HLL) Riemann solver, the contact discontinuity restoring HLLC Riemann solver, and the Roe Riemann solver, can be applied to solve the local Riemann problem. Since the upwind direction may not be perpendicular to the grid-aligned direction, here we use the rotated HLLC Riemann solver. The first example is the Mach 3 wind tunnel problem with step. The computational domain is $[0, 3] \times [0, 1]$ with a step of height 0.2 placed at 0.6 from the entrance. The inflow boundary condition is imposed at the left boundary, and supersonic outflow is applied at the right boundary. The upper and lower boundaries are treated as reflective boundaries. Initially, the primitive variables (ρ, u, v, p) are set as (1.4, 3, 0, 1). Figure 4.7 depicted the simulations using different CESE schemes with 1800×600 structured cartesian meshes. Both the CNI scheme and the upwind scheme can capture the shear layer instability that is missed in the result from a–α scheme.

The second example is the double Mach reflection problem. A Mach 10 shock propagates to the right and reflects over a solid wedge with an incline angle of 30°. A supersonic inflow boundary condition was implemented on the left boundary. Reflective and non-reflective boundary conditions were applied on the lower and upper boundary, respectively. The problem was solved using unstructured quadrilateral meshes with a mesh size of 1/400. Figure 4.8 compares the results by applying different schemes at computation time $t = 0.2$. All the three schemes can accurately describe the structures while the upwind scheme surpasses with finer resolved feature near the wall-adjacent jet.

(a) a-αCESE

(b) Rotated HLLC CESE

(c) CNI CESE
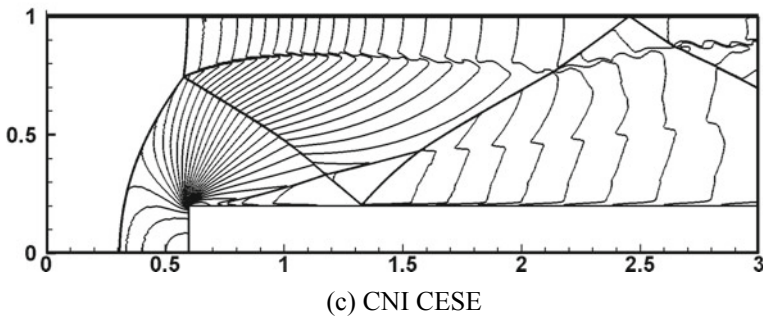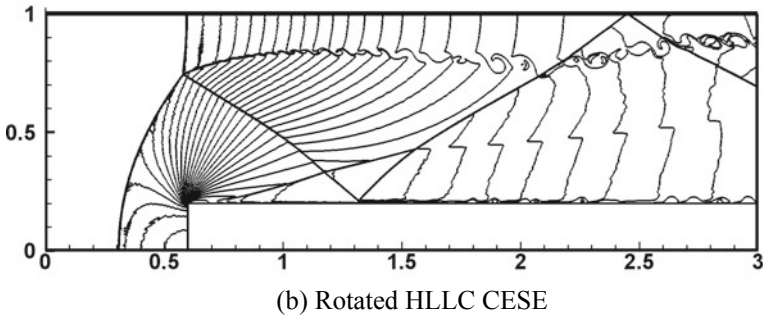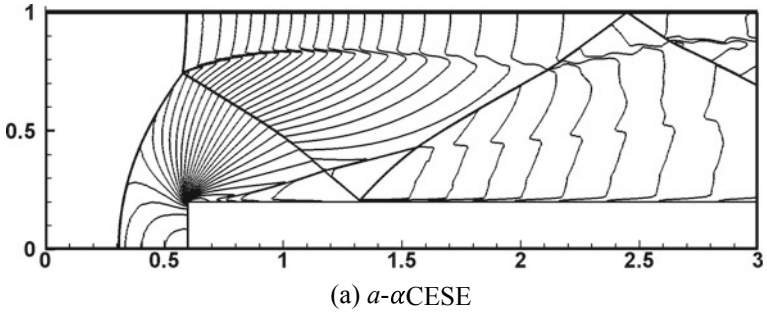
Fig. 4.7 Mach 3 wind tunnel with a step simulated by different CESE schemes with 1800×600 mesh grids: density contours at $t = 4.0$

Fig. 4.8 Double Mach
reflection problem computed
by different CESE schemes
with unstructured
quadrilateral meshes: density
contours at $t = 0.2$

(a) a-αCESE

(b) Rotated HLLC CESE

(c) CNI CESE
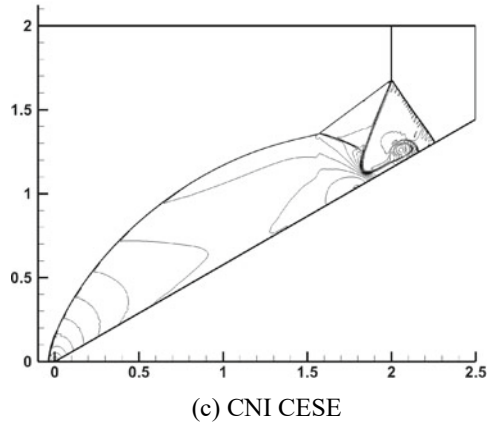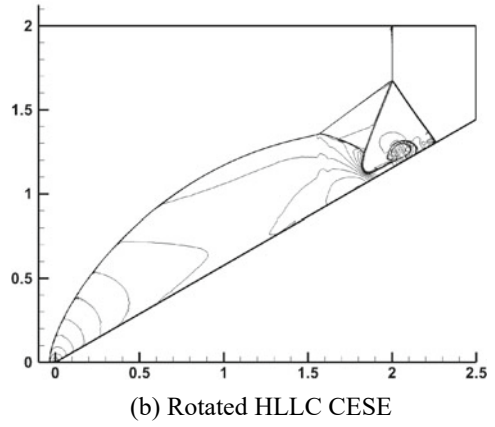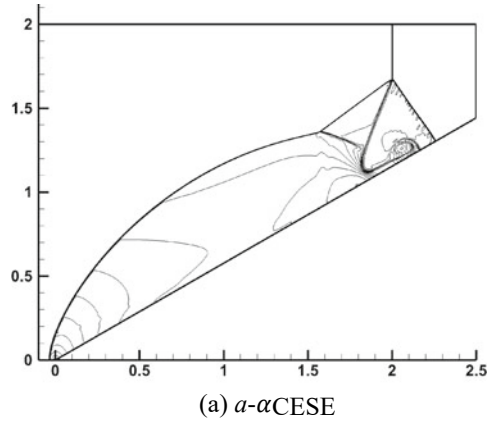
References

1. Chang, S. C., Wang, X. Y., & Chow, C. Y. (1999). The space-time conservation element and solution element method: A new high-resolution and genuinely multidimensional paradigm for solving conservation laws. *Journal of Computational Physics, 156*(1), 89–136.
2. Zhang, Z. C., Yu, S. J., & Chang, S. C. (2002). A space-time conservation element and solution element method for solving the two-and three-dimensional unsteady Euler equations using quadrilateral and hexahedral meshes. *Journal of Computational Physics, 175*(1), 168–199.
3. Wang, J. T., Liu, K. X., & Zhang, D. L. (2009). An improved CE/SE scheme for multi-material elastic–plastic flows and its applications. *Computers & fluids, 38*(3), 544–551.
4. Wang, G., Zhang, D. L., Liu, K. X., & Wang, J. T. (2010). An improved CE/SE scheme for numerical simulation of gaseous and two-phase detonations. *Computers & fluids, 39*(1), 168–177.
5. Chang, S.C., & Wang, X.Y. (2003). Multi-dimensional Courant number insensitive Euler solvers for applications involving highly nonuniform meshes. In *39th AIAA/ASME/SAE/ASEE Joint Propulsion Conference and Exhibit*.
6. Shen, H., & Wen, C. Y. (2016). A characteristic space–time conservation element and solution element method for conservation laws II. Multidimensional extension. *Journal of Computational Physics, 305*, 775–792.
7. Shen, H., Wen, C. Y., Liu, K. X., & Zhang, D. L. (2015). Robust high-order space–time conservative schemes for solving conservation laws on hybrid meshes. *Journal of Computational Physics, 281*, 375–402.
8. Shen, H., & Parsani, M. (2018). Positivity-preserving CE/SE schemes for solving the compressible Euler and Navier-Stokes equations on hybrid unstructured meshes. *Computer Physics Communications, 232*, 165–176.